nature communications

Article

https://doi.org/10.1038/s41467-024-47268-7

# Diffusion-rate sieving of propylene and propane mixtures in a cooperatively dynamic porous crystal

Received: 21 August 2023

Accepted: 26 March 2024

Published online: 04 April 2024

Check for updates

Yan Su[1], Ken-ichi Otake[2], Jia-Jia Zheng[3], Ping Wang[4], Qing Lin[5], Susumu Kitagawa[2] ✉ & Cheng Gu[1,4] ✉

Selective molecular recognition is an important alternative to the energy-intensive industrial separation process. Porous coordination polymers (PCPs) offer designing platforms for gas separation because they possess precise controllability over structures at the molecular level. However, PCPs-based gas separations are dominantly achieved using strong adsorptive sites for thermodynamic recognition or pore-aperture control for size sieving, which suffer from insufficient selectivity or sluggish kinetics. Developing PCPs that work at high temperatures and feature both high uptake capacity and selectivity is urgently required but remains challenging. Herein, we report diffusion-rate sieving of propylene/propane ($C_3H_6$/$C_3H_8$) at 300 K by constructing a PCP material whose global and local dynamics cooperatively govern the adsorption process via the mechanisms of the gate opening for $C_3H_6$ and the diffusion regulation for $C_3H_8$, respectively, yielding substantial differences in both uptake capacity and adsorption kinetics. Dynamic separation of an equimolar $C_3H_6$/$C_3H_8$ mixture reveals outstanding sieving performance with a $C_3H_6$ purity of 99.7% and a separation factor of 318.

Propylene ($C_3H_6$) is an important petrochemical feedstock to manufacture polypropylene that requires purity of propylene higher than 99.5%[1]. Industrial separation of propylene with propane ($C_3H_8$) is dominantly accomplished by energy-intensive cryogenic distillation[2], which motivates chemists to develop porous materials for adsorptive $C_3H_6$/$C_3H_8$ separation that is less energy-demanding. Porous coordination polymers (PCPs, or metal-organic frameworks) are attractive candidates as they provide precise controllability over the structures during adsorption and separation[3,4]. PCPs-based $C_3H_6$/$C_3H_8$ separation has been extensively studied and various separation mechanisms have been developed, such as isoreticular principle[5], pore space partition[6], open-metal sites (OMSs)[7–9], surface engineering[10], ligand modification[11], molecular docking[12,13], pore distortion[14], inverse separation[15], and size exclusion[16–18]. The essence of these approaches included the control of thermodynamics (Fig. 1a, b) and kinetics (Fig. 1c), with the size-exclusive sieving being an extreme scenario of the kinetically controlled process. Nevertheless, most of these approaches suffer from low to moderate separation factors or sluggish kinetics, even though rare reports have achieved both high selectivity and fast kinetics[19]. This is due to the similarity of $C_3H_6$ and $C_3H_8$ in physical properties and molecular size/shape (Supplementary Table 1), resulting in difficulty in designing pore systems with suitable environments and fine-tuned apertures with sub-nanometre precision.

Dynamic molecular sieving PCPs are expected to be advantageous if the targeted molecules could induce gate-opening at certain pressures[20]. However, the separation mechanism of such globally

[1]State Key Laboratory of Luminescent Materials and Devices, Institute of Polymer Optoelectronic Materials and Devices, South China University of Technology, Guangzhou 510640, P. R. China. [2]Institute for Integrated Cell-Material Sciences, Kyoto University, Yoshida, Sakyo-ku, Kyoto 606-8501, Japan. [3]Laboratory of Theoretical and Computational Nanoscience, National Center for Nanoscience and Technology, Chinese Academy of Sciences, Beijing 100190, P. R. China. [4]College of Polymer Science and Engineering, State Key Laboratory of Polymer Materials Engineering, Sichuan University, Chengdu 610065, P. R. China. [5]ReadCrystal Biotech Co., Ltd., Suzhou 215505, P. R. China. ✉e-mail: kitagawa@icems.kyoto-u.ac.jp; gucheng@scu.edu.cn

https://doi.org/10.1038/s41467-024-47268-7

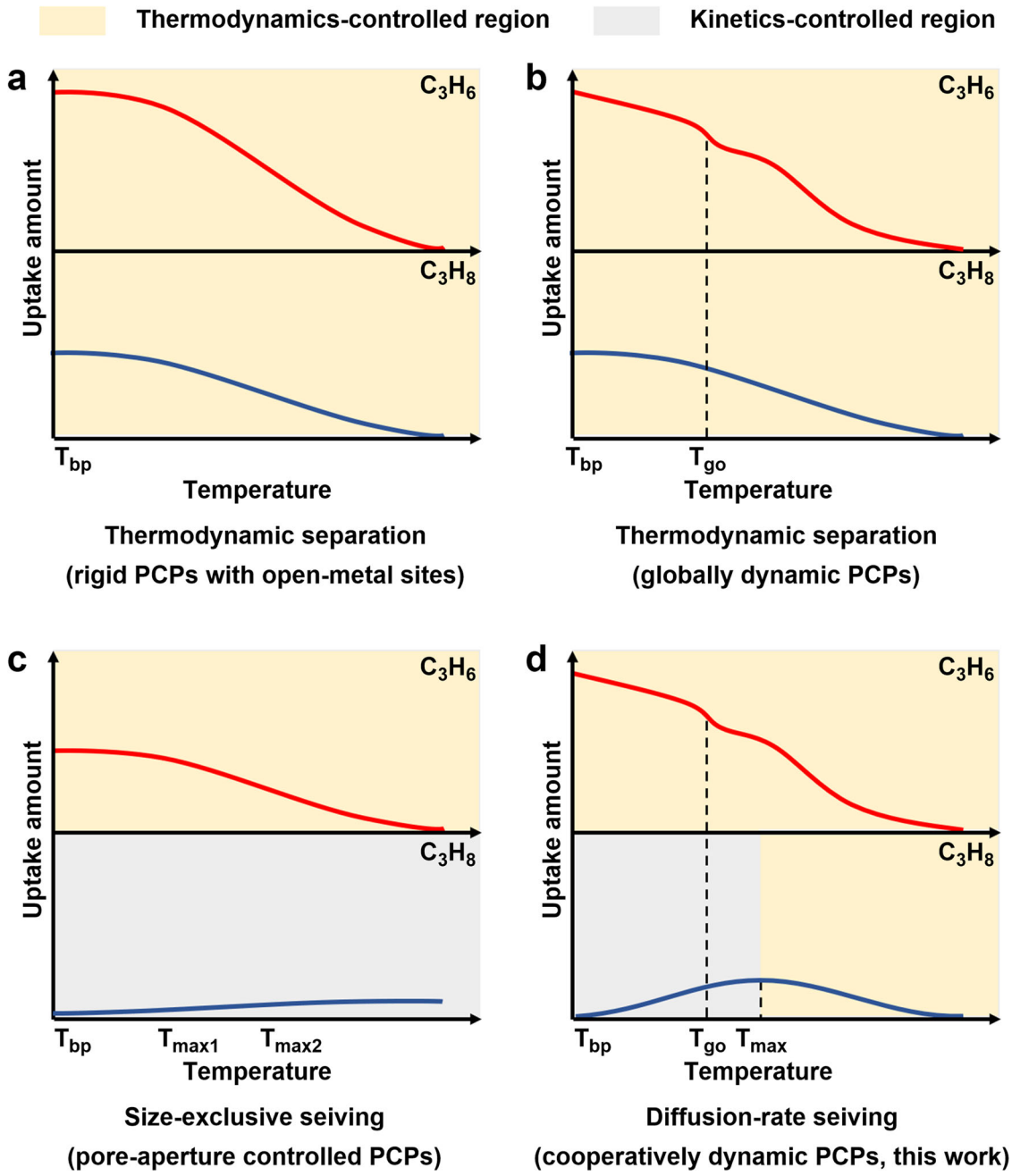


**Fig. 1 | The Diffusion-rate sieving mechanism using a cooperatively dynamic PCP to separate $C_3H_6$ and $C_3H_8$.** **a** Schematic representations of the $C_3H_6/C_3H_8$ adsorption isobars for the thermodynamic separation using rigid PCPs with open-metal sites. **b** Schematic representations of the $C_3H_6/C_3H_8$ adsorption isobars for the thermodynamic separation using globally dynamic PCPs. **c** Schematic representations of the $C_3H_6/C_3H_8$ adsorption isobars for the size-exclusive sieving using pore-aperture controlled PCPs. **d** Schematic representations of the $C_3H_6/C_3H_8$ adsorption isobars for the diffusion-rate sieving using a cooperatively dynamic PCP (this work); this mechanism involves a pore system featuring both gate-opening and diffusion-regulatory functionalities that can individually control the adsorption processes of different gases, thereby yielding substantial differences in both adsorption capacity and kinetics.

dynamic PCPs is still based on thermodynamics, with low-pressure gate-opening thresholds at low temperatures, which substantially move to higher pressures at high temperatures[21], thus rendering many flexible PCPs exhibiting separation performance by gate-opening at low temperatures but losing this ability at high temperatures. By contrast, locally dynamic PCPs feature rigid framework structures with locally movable substituents that respond to external stimuli such as temperature[22,23]. By designing the motive substituents at the pore apertures with various motion mechanisms, such as chemical-triggered adaptative pore[24], temperature-responsive pore apertures[25,26], and orthogonal-array pore system[19], locally dynamic PCPs have accomplished challenging gas separation. However, these PCPs encounter sluggish kinetics in the separation process because the thermodynamic equilibrium is difficult to achieve (Fig. 1c). Ideally, porous materials combining the advantages of global and local dynamic motions would offer a new type of separation, in which one gas triggers the gate-opening of the framework while its diffusion among the pores is unimpeded, whereas the other gas is not able to open the gate while its diffusion rate is lowered and regulated by the local dynamics of the framework. Thus far, such cooperative PCPs by means of combined global and local dynamic motions for efficient gas separation have yet to be demonstrated and accomplished.

Herein, we report efficient $C_3H_6/C_3H_8$ separation at 300 K by a diffusion-rate sieving mechanism, in which $C_3H_6$ and $C_3H_8$ in a PCP material exhibit over 60-fold differences in diffusion rates and thus ensuring the PCP to preferentially adsorb $C_3H_6$ and almost fully exclude $C_3H_8$. The essence of our mechanism is to construct a cooperative PCP, in which the global and local dynamics synergistically control the adsorption processes. $C_3H_6$ exhibits high gas-framework interaction energy and causes the PCP to globally deform accompanied by a gate-opening adsorption behavior, whereas the diffusion of $C_3H_8$ is regulated by the local motion of the ligand because the weak $C_3H_8$-PCP interaction renders the global structural change of PCP impossible (Fig. 1d). Consequently, the adsorptions of $C_3H_6$ and $C_3H_8$ at 300 K are individually governed by thermodynamics and kinetics, yielding remarkable $C_3H_6/C_3H_8$ selectivity, diffusion-rate difference, and $C_3H_6$ uptake amount, which make this separation mechanism distinct from the conventional size sieving with low $C_3H_6$ uptake and torpid kinetics. Diffusion-rate sieving from an equimolar $C_3H_6/C_3H_8$ mixture yields a separation factor of 318, $C_3H_6$ purity up to 99.7%, and $C_3H_6$ productivity of 19.5 L $kg^{-1}$.

## Results

### PCP synthesis and structural analysis

We designed a Cu-based PCP with an asymmetric, rhinoceros beetle-shape ligand comprising isophthalic acid and 5-(10-methoxy-5H-dibenzo[b,f]azepin-5-yl) (MODBAP) moieties (MODBAP-ipa; see Supplementary information and Supplementary Figs. 1–9), with the latter moiety exhibiting effective flip-flop local motion with flipping energy of 34.8 kJ $mol^{-1}$ (Supplementary Fig. 10). The as-synthesized PCP, namely, Cu(MODBAP) (termed **FDC–4**, FDC = flip-flop dynamic crystal) (Supplementary Figs. 11, 12, Supplementary Table 2, Supplementary Data 1), possessed a Kagomé-type layered structure with the neighboring layers stacking in a staggered mode; one hexagonal pore was horizontally surrounded by the framework linked by $Cu^{2+}$ paddle wheels and isophthalic groups, whereas six MODBAP moieties asymmetrically covered the pores from two vertical sides (Supplementary Fig. 13). Subsequently, **FDC–4** was subjected to solvent exchange and vacuum heating at 393 K to afford its activated phase (**FDC–4a**, Supplementary Figs. 14–18). The single-crystal structure of **FDC–4a** was determined by the continuous rotation electron diffraction (cRED) technique (Supplementary Figs. 16, 17, Supplementary Table 3). Activation gave rise to one-third of the OMSs on the $Cu^{2+}$ paddle wheels coordinating with the O atoms on MODBAP moieties in the neighboring layers (Fig. 2a), thereby transforming **FDC–4a** into a robust three-dimensional framework with one-dimensional helical pores (Fig. 2b), which possessed only one type of small diffusion gate, surrounded by two H atoms on benzene rings of the two MODBAP moieties with 3.76 Å distance (Fig. 2c). Therefore, the thermal flipping of MODBAP units was expected to enlarge the gate size to promote the gas diffusion at high temperatures and shrink the gate to block the gas diffusion at low temperatures (Fig. 2d).

### Gas sorption and in-situ PXRD

**FDC–4a** exhibited distinct adsorption behavior depending on the sizes of the investigated gases, as revealed by their adsorption isobars

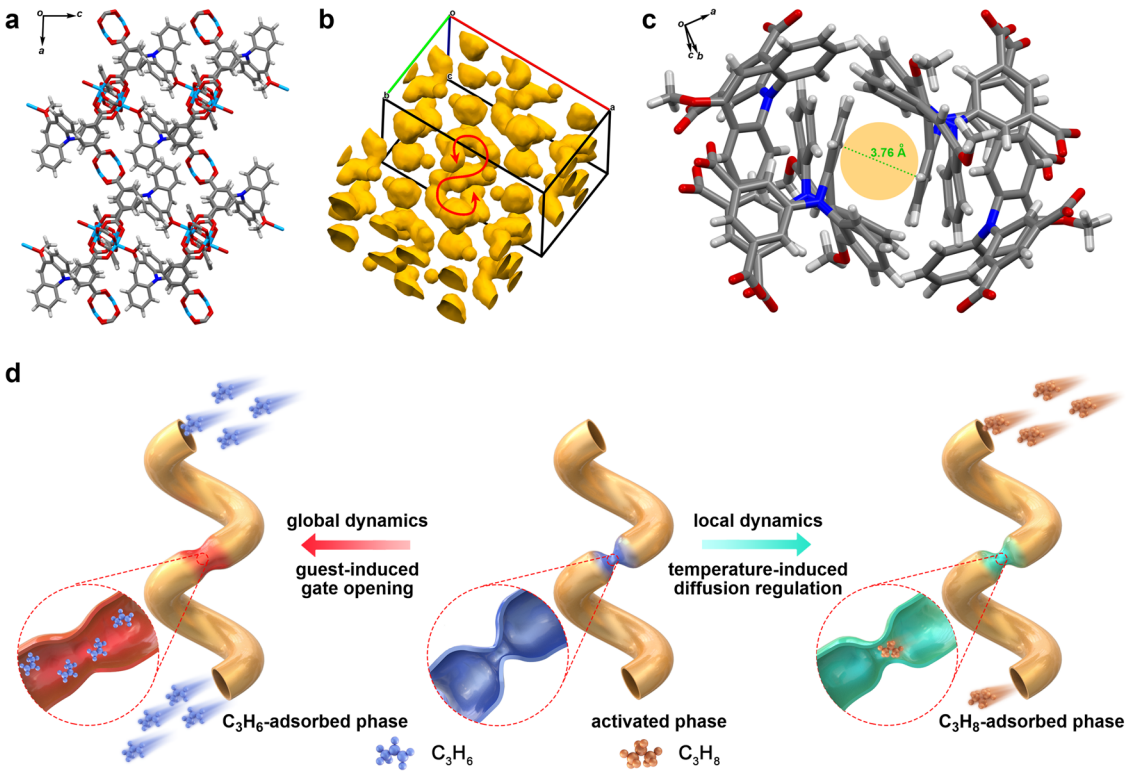


**Fig. 2 | Depiction of the PCP structure. a** The crystal structure of **FDC–4a** viewed along the *b* axis. Carbon, gray; nitrogen, blue; hydrogen, white; oxygen, red; copper, light blue. For clarity, the MODBAP moieties whose O atoms are uncoordinated with the OMSs of the $Cu^{2+}$ paddle wheels are omitted. **b** The void in **FDC–4a** visualized by a small probe radius of 1.2 Å. The void volume is 1594 $Å^3$ and corresponds to 12.3% of the unit-cell volume. The inner and outer surfaces of the pore are drawn in brown and yellow, respectively. The red arrow shows the helical pore. **c** The structure of the diffusion gate, which is surrounded by two H atoms on benzene rings of the two MODBAP moieties with a 3.76 Å distance. **d** Schematic diagram of the cooperatively dynamic PCP in this work. The PCP with one-dimensional (1D) transport pathways is constructed. The apertures are colored blue and red for the closed and open phases, respectively. In the closed phase, the pore entrances are smaller than the kinetic diameters of $C_3H_8$; hence, the pores are almost isolated, which regulates the diffusion of $C_3H_8$ by the thermal flipping of the gate moieties that slightly enlarge the gate (the apertures are colored green). In the open phase, the pore entrances become much larger because of the gate opening, and the pores open for $C_3H_6$ adsorption.

(Supplementary Fig. 19)[27,28]. In the cases of $CO_2$ and $C_2H_2$ whose kinetic diameters (3.30 Å) were smaller than the diffusion gate of **FDC–4a**, the adsorption amounts of the two gases monotonously decreased with increasing temperature from 200 to 370 K, indicating a thermodynamics-controlled process. By contrast, when the gases possessed kinetic diameters similar to ($N_2$ and CO, 3.64–3.80 Å) or larger than ($C_2H_4$ and $C_2H_6$, 4.16–4.44 Å) the diffusion gate, they showed volcano-type isobars that demonstrated domination of kinetics and thermodynamics at low (80 to 150 K for $N_2$/CO, 180 to 210 K for $C_2H_4$, and 190 to 270 K for $C_2H_6$) and high (160 to 370 K for $N_2$/CO, 220 to 370 K for $C_2H_4$, and 200 to 370 K for $C_2H_6$) temperatures[25], respectively. Remarkably, monotonously decreased and volcano-type isobars were observed for $C_3H_6$ and $C_3H_8$, respectively (Fig. 3a), evidencing that their adsorptions were governed by thermodynamical and diffusion-regulatory factors, respectively. Isotherm measurements at individual temperatures revealed the same trends with isobars (Supplementary Fig. 20). Therefore, the different adsorption behaviors of $C_3H_6$ and $C_3H_8$ suggested a high $C_3H_6/C_3H_8$ selectivity (Fig. 3a, Supplementary Table 4). More importantly, **FDC–4a** maintained a high $C_3H_6$ uptake of 122 $cm^3\ g^{-1}$ at 300 K and such a balance between uptake and selectivity catapulted **FDC–4a** to the region of ideal sieving[18]. Additionally, the isosteric heat ($Q_{st}$) value of $C_3H_6$ adsorption was calculated to be 35.0 kJ $mol^{-1}$ (Supplementary Fig. 21), which was lower than many of the $C_3H_6$-selective materials[4–19] (Supplementary Table 4) and thus indicating an easy regeneration in separation.

To unveil the structural change of **FDC–4a** during $C_3H_6$ and $C_3H_8$ adsorption, coincident in-situ powder X-ray diffraction (PXRD) patterns were recorded[29]. The $C_3H_6$-sorption isotherm at 240 K revealed a steep increase in the uptake amount at the low-pressure range (Fig. 3b) accompanied by the gate-opening behavior, as shown in the in-situ PXRD (Fig. 3c). The peaks attributed to the (002), (022), (22-2), (004), and (11-4) facets continuously shifted to lower angles, indicative of the increased distances of these facets, whereas the peaks belonging to the (020) and (310) facets merged into a new peak. These results indicated that the gate opening gradually and smoothly occurred, rather than the abrupt or stepped gate opening in many soft PCPs. We further collected the coincident in-situ isobar/PXRD patterns for $C_3H_6$ adsorption in the temperature range of 230 to 370 K (Supplementary Figs. 22, 23), showed temperature-responsive gating-opening behavior due to the thermodynamics-controlled change of gas-framework affinity. By contrast, $C_3H_8$ hardly caused the structural change of **FDC–4a**, as confirmed by both isotherm and isobar measurements (Fig. 3, b, d, Supplementary Figs. 24, 25). Therefore, its diffusion in **FDC–4a** was regulated by the pore apertures and exhibited volcano-type adsorption isobar due to the competition of thermodynamics and kinetics.

## Adsorption kinetics

To evaluate the adsorption kinetics for $C_3H_6$ and $C_3H_8$, we quantified the diffusion rate by Crank theory for every $C_3H_6$ or $C_3H_8$ adsorption plot in the 240 to 360 K range (supplementary information). This allowed us to produce the global $P$–$D_s/R^2$–$V$ and $T$–$D_s/R^2$–$V$ landscapes, where $P$ (relative pressure), $T$ (K), $V$ ($cm^3\ g^{-1}$), and $D_s$ ($R^2\ s^{-1}$) denote the pressure, temperature, uptake volume, and diffusion rate, respectively, where R represents the radius of a PCP particle (Fig. 4a, b, Supplementary Fig. 26). Both $C_3H_6$ and $C_3H_8$ exhibited increased diffusion rates along with pressure and temperature. At the beginning of the $C_3H_6$ adsorption at 240, 260, and 280 K, the $C_3H_6$ diffusion was

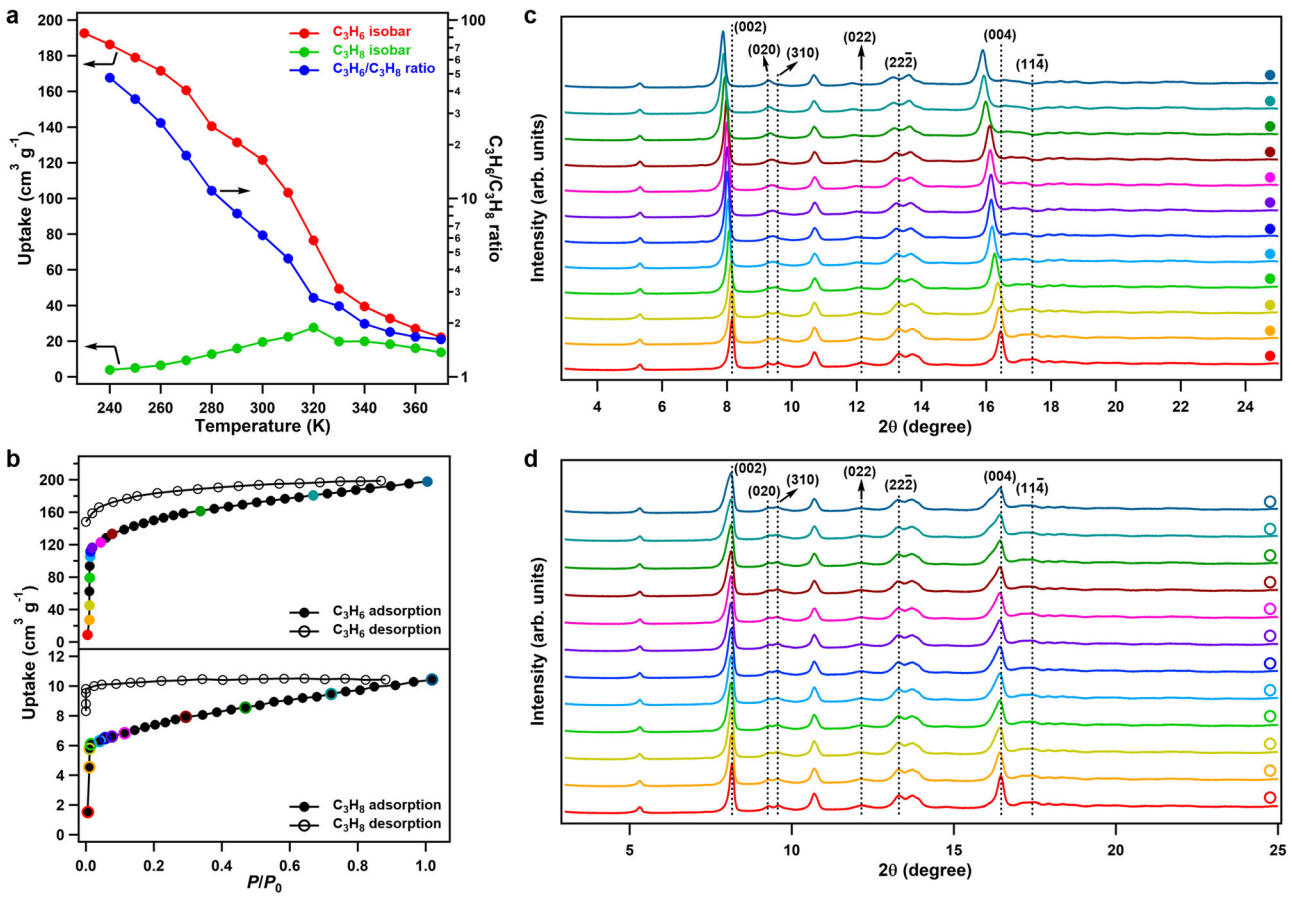


**Fig. 3 | Gas adsorption and in-situ PXRD. a** $C_3H_6$ and $C_3H_8$ adsorption isobars at 1 bar and the $C_3H_6/C_3H_8$ uptake ratio. **b** $C_3H_6$ and $C_3H_8$ sorption isotherms at 240 K. **c** Coincident in-situ adsorption/PXRD patterns during $C_3H_6$ adsorption measured at 240 K at given equilibrium pressures. **d** Coincident in-situ adsorption/PXRD patterns during $C_3H_8$ adsorption measured at 240 K at given equilibrium pressures.

https://doi.org/10.1038/s41467-024-47268-7

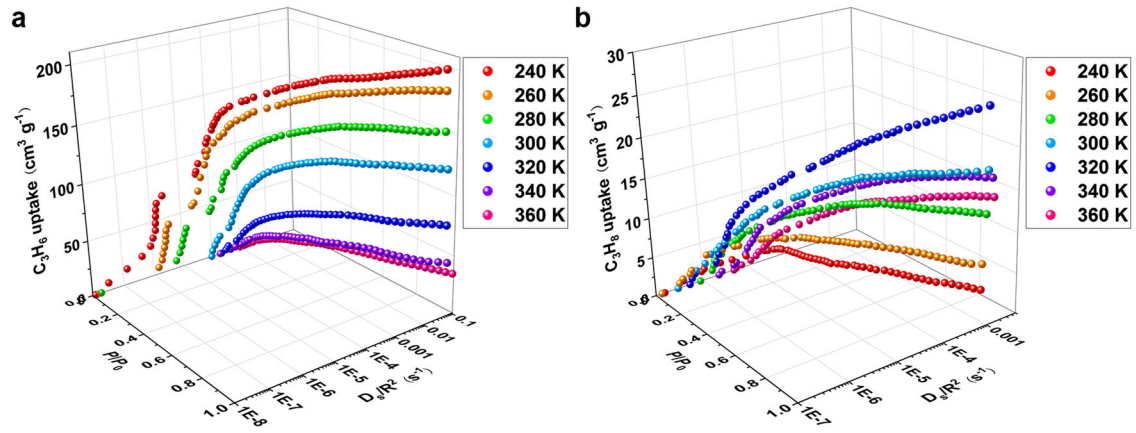


**Fig. 4 | Diffusion rates of $C_3H_6$ and $C_3H_8$ in FDC−4a. a** Global pressure–diffusion-rate–adsorption-amount ($P$–$D_s/R^2$–$V$) landscape for **FDC−4a** adsorbing $C_3H_6$, where R denotes the radius of a PCP particle. **b** $P$–$D_s/R^2$–$V$ landscape for **FDC−4a** adsorbing $C_3H_8$.

largely hindered with substantially low $D_s$ values of less than $10^{-5}$ $R^2$ $s^{-1}$. When the pressure was increased to reach the gate opening, the $C_3H_6$ diffusion rates were abruptly increased by about 10 folds. Afterward, the $C_3H_6$ diffusion rates markedly increased with pressure. At the relative pressure close to 1.0, the $C_3H_6$ diffusion rates were $5.05 \times 10^{-2}$ and $7.09 \times 10^{-2}$ $R^2$ $s^{-1}$ at 240 and 300 K, respectively. By contrast, the $C_3H_8$ diffusion rates smoothly increased with pressure without abrupt increment observed, and the $D_s$ values at the relative pressure close to 1.0 were $8.73 \times 10^{-4}$ and $1.13 \times 10^{-3}$ $R^2$ $s^{-1}$ at 240 and 300 K, respectively. $C_3H_6$ exhibited diffusion rates of 57.8- and 62.7-folds of those of $C_3H_8$ at 240 and 300 K, respectively, indicating that the substantial differences could promote effective diffusion-rate sieving of $C_3H_6/C_3H_8$.

## VT-PXRD and computational studies

To understand the adsorption behavior from a structural perspective, synchrotron variable-temperature PXRD (VT-PXRD) patterns for **FDC−4a** were recorded, which revealed inconspicuous peak shifts to lower angles with increasing temperature under vacuum (Supplementary Figs. 27, 28). Taking the peak attributed to the (002) plane as an example, the peak shifted by 0.042° from 90 to 375 K. This slight structural change was apparently different from the global dynamics of **FDC−4a** showing obvious PXRD shifts, thereby demonstrating a temperature-responsive local dynamics in **FDC−4a**. The peak shift indicated the expansion of the [002] axis. Because there were two MODBAP moieties lying on the (002) plane, this small expansion could be induced by the thermal flipping of MODBAP moieties, which enlarged the diffusion gates to facilitate adsorption (Supplementary Fig. 29).

Density functional theory calculations were carried out to understand the difference between $C_3H_6$ and $C_3H_8$ adsorption and diffusion in **FDC−4a**. Because there was little change in lattices of **FDC−4a** during a low-amount $C_3H_6$ adsorption and overall $C_3H_8$ adsorption, we only considered adsorptions of these two gases in the activated phase of **FDC−4a** to elucidate the reason for the high selectivity of **FDC−4a** towards $C_3H_6/C_3H_8$ separation. Two different adsorption sites were found for both $C_3H_6$ and $C_3H_8$ in **FDC−4a** (Supplementary Fig. 30, see supplementary methods for computational details). The binding energies (BEs) of gas molecules with **FDC−4a** at these adsorption sites were calculated as –47.3 (site I) and –34.9 kJ $mol^{-1}$ (site II) for $C_3H_6$ and –48.7 (site I) and –23.2 kJ $mol^{-1}$ (site II) for $C_3H_8$ (Supplementary Table 5). The more negative BE of $C_3H_6$ at site II indicated its stronger affinity to **FDC−4a** than $C_3H_8$, consistent with the larger adsorption amount of $C_3H_6$ than that of $C_3H_8$ at high temperatures such as 360 K. On the contrary, the similar BE values of $C_3H_6$ and $C_3H_8$ at the site I suggested that the adsorption amount of $C_3H_8$ should be comparable to that of $C_3H_6$ at very low loadings (<20 mL $g^{-1}$), which was seemingly against the experimental observation. This is because the kinetic factor plays an important role in the selective adsorption of $C_3H_6$ over $C_3H_8$, as discussed above; the diffusion rate of $C_3H_8$ is so low that the $C_3H_8$ transport in **FDC−4a** is significantly hindered, thereby its adsorption amount is much lower than that in the equilibrium state. To further clarify this point, we calculated the diffusion barriers of $C_3H_6$ and $C_3H_8$ in **FDC−4a** (Supplementary Fig. 31). As expected, the calculated diffusion barrier of $C_3H_8$ was as high as 77.3 kJ $mol^{-1}$, which impeded the transport of $C_3H_8$ even near room temperature. On the other hand, the diffusion barrier for $C_3H_6$ was approximately 60.0 kJ $mol^{-1}$, which was much smaller than that of $C_3H_8$ diffusion, suggesting that $C_3H_6$ could enter the pores of **FDC−4a** more easily than $C_3H_8$. These results indicate that the adsorption and transport of $C_3H_6$ into **FDC−4a** are more favorable than those of $C_3H_8$ from the viewpoints of adsorption thermodynamics and kinetics, essentially promoting the $C_3H_6/C_3H_8$ separation performance.

## Mixed gas separation

The sorption mechanism inspired us to perform dynamic separation of the $C_3H_6/C_3H_8$ mixtures by a temperature-programmed desorption (TPD) protocol (Supplementary Figs. 32, 33); the experiments were carried out at 300 K with an equimolar $C_3H_6/C_3H_8$ mixture. **FDC−4a** preferentially adsorbed $C_3H_6$ from the $C_3H_6/C_3H_8$ mixture within a short exposure time of 1 h, resulting in a remarkable $C_3H_6$ enrichment with a concentration as high as 99.7% in the adsorbed phase (Fig. 5a, Supplementary Fig. 34) and a separation factor of 318 (Fig. 5b). The productivity of $C_3H_6$ with 99.7% purity in a single adsorption-desorption cycle, estimated from the $C_3H_6$ TPD spectra and the calibration curve, was 19.5 L $kg^{-1}$, which was comparable to JNU-3a (34.2 L $kg^{-1}$, 99.5% purity)[19], KAUST-7 (16.3 L $kg^{-1}$, 90.0% purity)[16], and Y-abtc (1.3 L $kg^{-1}$, 90.0% purity)[6]. These results suggested the potential of **FDC−4a** for isolating $C_3H_6$ from the industrial equimolar $C_3H_6/C_3H_8$ mixture. The separation factor decreased with prolonged exposure time (Supplementary Figs. 34–39), indicating that $C_3H_6$ was adsorbed substantially faster than $C_3H_8$ and occupied most of the available space, which excluded $C_3H_8$ by the diffusion-rate sieving mechanism as a consequence. Remarkably, **FDC−4a** exhibited high separation performance over a wide range of feed-gas compositions (Fig. 5a, Supplementary Figs. 40–49). Even when the mixture contained ultra-low $C_3H_6$ of 5 mol%, the $C_3H_6$ concentration in the adsorbed phase was 99.4%, corresponding to an outstanding separation factor of 3078 (Fig. 5b), demonstrating that the diffusion-rate sieving is key to achieving exceptional selectivity.

Dynamic column breakthrough experiments indicate practical aspects of the separation capability of **FDC−4a**. Initially, an equimolar

https://doi.org/10.1038/s41467-024-47268-7

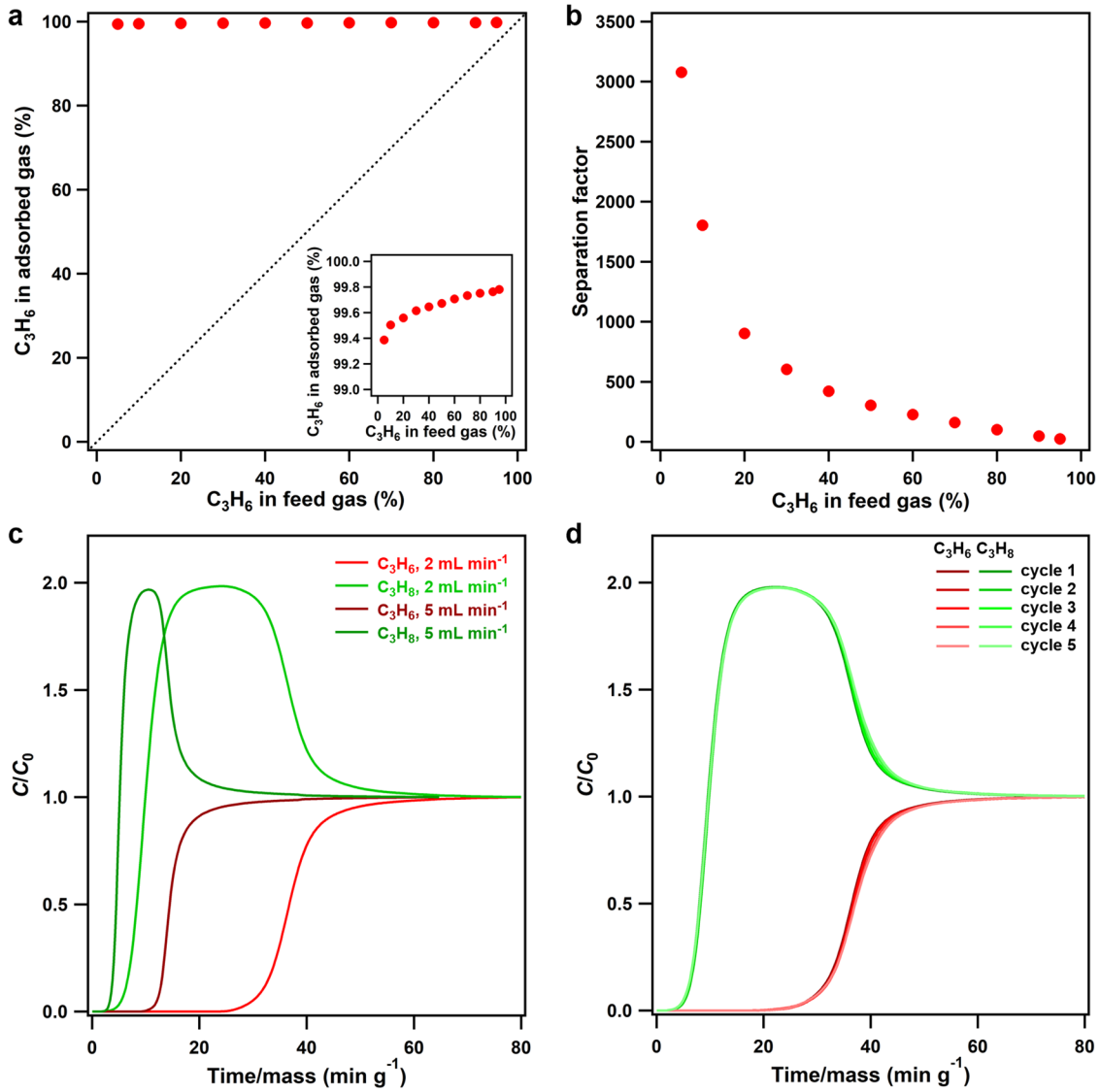


**Fig. 5 | Mixed gas separation. a** McCabe–Thiele diagram for $C_3H_6/C_3H_8$ separation by **FDC–4a** at 300 K, with the dashed line representing the theoretical behavior of showing no selectivity. The inset is the enlarged Y-axis showing the $C_3H_6$ fractions in the adsorbed phase. **b** The correlation between $C_3H_6$ concentration in the feed gas and the separation factor for **FDC–4a**. **c** The breakthrough curve of an equimolar $C_3H_6/C_3H_8$ mixture (total flow rate of 4.0 and 10.0 mL min$^{-1}$, respectively) on **FDC–4a** at 300 K. *C* and $C_0$ are the concentrations of each gas at the outlet and inlet, respectively. **d** The breakthrough curves for a cycling test of an equimolar $C_3H_6/C_3H_8$ mixture (total flow rate of 4.0 mL min$^{-1}$) on **FDC–4a** at 300 K.

$C_3H_6/C_3H_8$ mixture was passed through the **FDC–4a** column with a flow rate of 4 mL min$^{-1}$. The mixture was efficiently separated with the $C_3H_6$ purity and productivity obtained from the desorption curve of 99.1% and 19.5 L kg$^{-1}$, respectively (Fig. 5c, Supplementary Fig. 50). **FDC–4a** retained good separation performance with the equimolar $C_3H_6/C_3H_8$ mixture even under a much higher flow rate of 10 mL min$^{-1}$, with the $C_3H_6$ purity and productivity of 98.9% and 21.2 L kg$^{-1}$, respectively (Fig. 5c, Supplementary Fig. 51), indicating the fast kinetics during separation. On the other hand, **FDC–4a** was adaptable for separating $C_3H_6/C_3H_8$ mixtures with varied compositions; the $C_3H_6/C_3H_8$ mixtures with molar ratios of 10:90 and 90:10 were also separated by **FDC–4a** (Supplementary Figs. 52–55). The $C_3H_6$ productivity under different desorption conditions was also investigated; under the desorption temperatures of 393 and 300 K, the $C_3H_6$ productivity was 19.5 (99.1% purity) and 19.2 (99.1% purity) L kg$^{-1}$, respectively (Supplementary Fig. 56), demonstrating that the physisorption with low gas-framework affinity in **FDC–4a** was beneficial for energy-saving production of $C_3H_6$. Finally, **FDC–4a** exhibited stability under continuous 5 breakthrough cycles (Fig. 5d), suggesting its potential in real separation applications.

## Discussion

This work demonstrates the efficient diffusion-rate sieving of $C_3H_6/C_3H_8$ in a PCP material by manipulating the global and local dynamics of the framework. The TPD experiments reveal kinetics-based sieving separation of an equimolar $C_3H_6/C_3H_8$ mixture at 300 K with a separation factor of 318, $C_3H_6$ purity up to 99.7%, and $C_3H_6$ productivity of 19.5 L kg$^{-1}$ in a single adsorption-desorption cycle. These striking separation performances are ascribed to the underlying mechanism, which is realized by the cooperation of global dynamics of the framework upon $C_3H_6$ adsorption and local dynamics of gate constituents to regulate $C_3H_8$ diffusion. This design rationale can be more broadly suitable for various porous materials for efficient gas separation.

## Methods

### Synthesis of MODBAP-ipa ligand

**Synthesis of dimethyl 5-(10-methoxy-5*H*-dibenzo[*b,f*]azepin-5-yl) isophthalate (1).** Dimethyl 5-iodoisophthalate (19.20 g, 60.0 mmol, 1.2 eq.), 10-methoxy-5*H*-dibenzo[*b,f*]azepine (11.16 g, 50.0 mmol, 1.0 eq.), 2-dicyclohexylphosphino-2′,4′,6′-triisopropylbiphenyl (XPhos, 1.19 g, 2.5 mmol, 0.05 eq.), tris(dibenzylideneacetone)dipalladium(0) (1.37 g, 1.5 mmol, 0.03 eq.), cesium carbonate (32.58 g, 100.0 mmol, 2.5 eq.), and toluene (200 mL) were placed in a flask whose inner gas was replaced by $N_2$. The mixture was stirred at 115 °C for 48 h. After cooling down to room temperature, the reaction mixture was filtered through Celite®. The filtrate was diluted with ethyl acetate (200 mL) and washed with water. The organic phase was dried over $MgSO_4$, filtered, and evaporated under reduced pressure. The residue was purified by column chromatography ($SiO_2$, ethyl acetate/*n*-hexane with the ratio changing from 3 to 6%) to give **1** (11.22 g, yield = 54%) as a light-yellow solid. $^1$H NMR (500 MHz, DMSO-$d_6$): δ (ppm) = 7.80 (2H, d, $J$ = 11.5 Hz, Ph $C_2$-*H* and MODBAP $C_6$-*H*), 7.70 (1H, t, $J$ = 7.6 Hz, MODBAP $C_9$-*H*), 7.60 (1H, d, $J$ = 7.9 Hz, MODBAP $C_8$-*H*), 7.55 (3H, dd, $J$ = 15.5, 6.6 Hz, MODBAP $C_{1,4,7}$-*H*), 7.47 (1H, t, $J$ = 7.5 Hz, MODBAP $C_2$-*H*), 7.42 (1H, t, $J$ = 7.4 Hz, MODBAP $C_3$-*H*), 7.04 (2H, s, Ph $C_{4,6}$-*H*), 6.29 (1H, s, MODBAP $C_{11}$-*H*), 3.75 (9H, s, -$CO_2CH_3$ and -$OCH_3$); $^{13}$C NMR (126 MHz, DMSO-$d_6$): δ (ppm) = 165.97, 155.83, 149.06, 135.73, 133.89, 131.97, 131.14, 130.93, 129.73, 129.40, 128.89, 128.61, 128.46, 128.20, 119.35, 115.67, 102.71, 55.94, 52.81; MALDI-TOF-MS: calcd. $m/z$ = 415.1420; found $m/z$ = 415.654.

**Synthesis of 5-(10-methoxy-5*H*-dibenzo[*b,f*]azepin-5-yl)isophthalic acid (MODBAP-ipa).** To the THF/MeOH (200 mL, 1/1 v/v) solution containing **1** (10.0 g, 25.9 mmol) was added 2 M NaOH aqueous solution (200 mL, 400 mmol) and the system was reflexed for 16 h. After cooling to 0 °C, the reaction mixture was acidified with concentrated HCl. The precipitate was collected by filtration, washed with water, and then dried under reduced pressure at 60 °C to give **MODBAP-ipa** (8.0 g, yield = 90%) as a white solid. $^1$H NMR (500 MHz, DMSO-$d_6$): δ (ppm) = 13.03 (2H, s, -$CO_2H$), 7.83-7.75 (2H, m, Ph $C_2$-*H* and MODBAP $C_6$-*H*), 7.68 (1H, t, $J$ = 7.6 Hz, MODBAP $C_9$-*H*), 7.59 (1H, d, $J$ = 7.9 Hz, MODBAP $C_8$-*H*), 7.53 (3H, dt, $J$ = 15.6, 7.8 Hz, MODBAP $C_{1,4,7}$-*H*), 7.46 (1H, t, $J$ = 7.4 Hz, MODBAP $C_2$-*H*), 7.40 (1H, t, $J$ = 7.4 Hz, MODBAP $C_3$-*H*), 7.03 (2H, s, Ph $C_{4,6}$-*H*), 6.29 (1H, s, MODBAP $C_{11}$-*H*), 3.76 (3H, s, -$OCH_3$); $^{13}$C NMR (126 MHz, DMSO-$d_6$): δ = 167.21, 155.84, 148.88, 142.12, 140.43, 135.81, 133.99, 132.15, 131.92, 130.89, 129.89, 129.55, 128.84, 128.56, 128.32, 128.08, 115.76, 102.78, 55.94; MALDI-TOF-MS: calcd. $m/z$ = 387.1107; found $m/z$ = 387.603.

### Synthesis of FDC−4

Firstly, 50 mg (0.13 mmol) **MODBAP-ipa** was dissolved in 6 mL DMF at room temperature. An aqueous solution (4 mL) of $Cu(NO_3)_2{\cdot}3H_2O$ (62.4 mg, 0.26 mmol) was added to the above solution. Then the mixture was heated at 80 °C for 24 h. **FDC−4** was obtained as green lamellar crystals with sizes up to several hundreds of micrometers (70 mg, yield = 65%). The crystals were filtered, washed with DMF (10 mL, 3 times) and $H_2O$ (10 mL, 3 times), and dried in air. The as-synthesized **FDC−4** was characterized by infrared spectra (Supplementary Fig. 12). The adsorption peak of the stretching vibration of the C = O double bond shifted to a low wavenumber, indicative of the coordination bond formation in **FDC−4**.

### Solvent exchange and activation of FDC−4

To measure the adsorption property of **FDC−4**, we exchanged the guest and coordination solvents (DMF) with methanol by soaking **FDC−4** in methanol at 60 °C for 7 days. Every 24 h the methanol was replaced by a new one. After the solvent exchange, the exchanged **FDC−4** was dried under vacuum at 60 °C for 3 h. $^1$H NMR confirmed that the DMF in the exchanged **FDC−4** was exchanged by methanol (Supplementary Fig. 14). TG curve showed that the framework of the exchanged **FDC−4** was thermally stable until 170 °C (Supplementary Fig. 15). Thus, we activated the exchanged **FDC−4** at 120 °C for 11 h to afford **FDC−4a**; this temperature ensured the complete removal of the solvents meanwhile excluding the possibility of framework decomposition.

## Data availability

Source data are provided with the study. All other information can be obtained from the corresponding author upon request. The X-ray crystallographic coordinates for structures reported in this study have been deposited at the Cambridge Crystallographic Data Centre (CCDC), under deposition numbers 2236283-2236284. These data can be obtained free of charge from The Cambridge Crystallographic Data Centre via www.ccdc.cam.ac.uk/data_request/cif. Source data are provided with this paper.

## References


1. Järvelin, H. & Fair, J. R. Adsorptive separation of propylene-propane mixtures. *Ind. Eng. Chem. Res.* **32**, 2201–2207 (1993).
2. Christopher, C. C. E., Dutta, A., Farooq, S. & Karimi, I. A. Process synthesis and optimization of propylene/propane separation using vapor recompression and self-heat recuperation. *Ind. Eng. Chem. Res.* **56**, 14557–14564 (2017).
3. Wilmer, C. E. et al. Large-scale screening of hypothetical metal-organic frameworks. *Nat. Chem.* **4**, 83–89 (2012).
4. Peng, Y.-L. et al. Efficient propyne/propadiene separation by microporous crystalline physiadsorbents. *Nat. Commun.* **12**, 5768 (2021).
5. Xie, Y. et al. Optimal binding affinity for sieving separation of propylene from propane in an oxyfluoride anion-based metal-organic framework. *J. Am. Chem. Soc.* **145**, 2386–2394 (2023).
6. Wang, H. et al. Tailor-made microporous metal-organic frameworks for the full separation of propane from propylene through selective size exclusion. *Adv. Mater.* **30**, 1805088 (2018).
7. Ding, Q. & Zhang, S. Recent advances in the development of metal-organic frameworks for propylene and propane separation. *Energy Fuels* **36**, 7337–7361 (2022).
8. Xie, Y., Shi, Y., Cui, H., Lin, R.-B. & Chen, B. Efficient separation of propylene from propane in an ultramicroporous cyanide-based compound with open metal sites. *Small Struct* **3**, 2100125 (2022).
9. Bae, Y.-S. et al. High propene/propane selectivity in isostructural metal-organic frameworks with high densities of open metal sites. *Angew. Chem. Int. Ed.* **51**, 1857–1860 (2012).
10. Bloch, E. D. et al. Hydrocarbon separations in a metal-organic framework with open Iron(II) coordination sites. *Science* **335**, 1606–1610 (2012).
11. Wang, Y. et al. Selective aerobic oxidation of a metal-organic framework boosts thermodynamic and kinetic propylene/propane selectivity. *Angew. Chem. Int. Ed.* **58**, 7692–7696 (2019).
12. Liu, D. et al. Scalable green synthesis of robust ultra-microporous Hofmann clathrate material with record $C_3H_6$ storage density for efficient $C_3H_6/C_3H_8$ separation. *Angew. Chem. Int. Ed.* **62**, e202218590 (2023).
13. Li, J. et al. Purification of propylene and ethylene by a robust metal-organic framework mediated by host-guest interactions. *Angew. Chem. Int. Ed.* **60**, 15541–15547 (2021).
14. Yu, L. et al. Pore distortion in a metal-organic framework for regulated separation of propane and propylene. *J. Am. Chem. Soc.* **143**, 19300–19305 (2021).
15. Zhang, P. et al. Ultramicroporous material based parallel and extended paraffin nano-trap for benchmark olefin purification. *Nat. Commun.* **13**, 4928 (2022).
16. Cadiau, A., Adil, K., Bhatt, P. M., Belmabkhout, Y. & Eddaoudi, M. A metal-organic framework–based splitter for separating propylene from propane. *Science* **353**, 137–140 (2016).

17. Dong, Q. et al. Confining water nanotubes in a $Cu_{10}O_{13}$-based metal-organic framework for propylene/propane separation with record-high selectivity. *J. Am. Chem. Soc.* **145**, 8043–8051 (2023).
18. Liang, B. et al. An ultramicroporous metal-organic framework for high sieving separation of propylene from propane. *J. Am. Chem. Soc.* **142**, 17795–17801 (2020).
19. Zeng, H. et al. Orthogonal-array dynamic molecular sieving of propylene/propane mixtures. *Nature* **595**, 542–548 (2021).
20. Horike, S., Shimomura, S. & Kitagawa, S. Soft porous crystals. *Nat. Chem.* **1**, 695–704 (2009).
21. Sen, S. et al. Cooperative bond scission in a soft porous crystal enables discriminatory gate opening for ethylene over ethane. *J. Am. Chem. Soc.* **139**, 18313–18321 (2017).
22. Zhang, J.-P. & Chen, X.-M. Exceptional framework flexibility and sorption behavior of a multifunctional porous cuprous triazolate framework. *J. Am. Chem. Soc.* **130**, 6010–6017 (2008).
23. Gao, Q., Xu, J., Cao, D., Chang, Z. & Bu, X.-H. A rigid nested metal-organic framework featuring a thermoresponsive gating effect dominated by counterions. *Angew. Chem. Int. Ed.* **55**, 15027–15030 (2016).
24. Katsoulidis, A. P. et al. Chemical control of structure and guest uptake by a conformationally mobile porous material. *Nature* **565**, 213–217 (2019).
25. Gu, C. et al. Design and control of gas diffusion process in a nanoporous soft crystal. *Science* **363**, 387–391 (2019).
26. Su, Y. et al. Separating water isotopologues using diffusion-regulatory porous materials. *Nature* **611**, 289–294 (2022).
27. Fernandez, C. A., Liu, J., Thallapally, P. K. & Strachan, D. M. Switching Kr/Xe selectivity with temperature in a metal–organic framework. *J. Am. Chem. Soc.* **134**, 9046–9049 (2012).
28. Wang, H. et al. Crystallizing atomic xenon in a flexible MOF to probe and understand its temperature-dependent breathing behavior and unusual gas adsorption phenomenon. *J. Am. Chem. Soc.* **142**, 20088–20097 (2020).
29. Carrington, E. J. et al. Solvent-switchable continuous-breathing behaviour in a diamondoid metal–organic framework and its influence on $CO_2$ versus $CH_4$ selectivity. *Nat. Chem.* **9**, 882–889 (2017).

## Acknowledgements

This work was supported by the National Natural Science Foundation of China (21975078), the Fundamental Research Funds for the Central Universities, the start-up foundation of Sichuan University, the KAKENHI Grant-in-Aid for Specially Promoted Research (JP25000007), and Scientific Research (S) (JP22H05005) from the Japan Society of the Promotion of Science (JSPS). We thank the iCeMS analysis center for access to the analytical instruments.

## Author contributions

Y.S. performed experiments associated with molecular synthesis, crystal growth, gas sorption, and gas separation. K.O. and P.W. conducted single-crystal and powder XRD studies and structure analyses. J.Z. carried out calculation studies. Q.L. performed cRED measurements and solved the structure of the activated phase. C.G. and S.K. conceived the project and directed the research. All authors contributed to the writing and editing of the manuscript.

## Competing interests

The authors declare no competing interests.

## Additional information

**Supplementary information** The online version contains supplementary material available at https://doi.org/10.1038/s41467-024-47268-7.

**Correspondence** and requests for materials should be addressed to Susumu Kitagawa or Cheng Gu.

**Peer review information** *Nature Communications* thanks Hoi Ri Moon and the other, anonymous, reviewer(s) for their contribution to the peer review of this work. A peer review file is available.